Imaging throughput of compact handheld microscopes for quantitative single cell studies

SOPHIE BULLOCH [1,ǂ], TIENAN XU [1,2,ǂ], DAVID HERRMANN[3,4,5], PAUL TIMPSON[3,4,5], TRI GIANG PHAN[3], YEAN JIN LIM [1,2,3,*] , WOEI MING LEE[1,2,3,*,ǂ]

[1]*Division of Genome Science and Cancer, John Curtin School of Medical Research, Australian National University, Canberra, ACT 2601*

[2]*Ability Optics Pty Ltd, Dickson, 490 Northbourne Avenue ACT 2602*

[3]*ACRF INCITe Centre – Garvan Institute of Medical Research, Sydney, NSW 2010, Australia*

[4]*Cancer Ecosystems Program, Garvan Institute of Medical Research and The Kinghorn Cancer Centre, Darlinghurst, New South Wales, Australia*

[5]*School of Clinical Medicine, UNSW Medicine & Health, St Vincent's Healthcare Clinical Campus, Faculty of Medicine and Health, UNSW Sydney, Kensington, New South Wales, Australia*

ǂ *Co-first Author*
**Co-Corresponding Author: daniel.lim@anu.edu.au,steve.lee@anu.edu.au*

Abstract: Incuscopes, incubator-compatible microscopes, are crucial for live single-cell imaging studies that spans several hours to days. However, traditional microscopy prioritize high-resolution imaging performance over throughput, neglecting efficient live-cell image sampling. This study challenges existing spatial bandwidth product (field of view/optical resolution) criteria for image sampling for live cells. We demonstrate that imaging throughput is fundamentally determined by the minimal pixel count necessary to adequately resolve single cells across the field of view, not spatial bandwidth product. Using an off-the-shelf handheld microscope (5MP, ~0.03 NA) and a scientific microscope (8MP, 4x, 0.4 NA), we revealed a striking disparity. Contrary to expectations, the handheld microscope exhibited ~4-fold higher imaging throughput, highlighting oversampling inherent in many scientific microscopes. This efficiency stems from a more optimized pixel-to-cell ratio for throughput. We validated this concept by deploying the handheld microscopes within a compact 30-liter incubator, enabling continuous imaging over 40 hours using open-source Micro-Manager. A series of experiments, including cell counting, tracking, division, migration, and spheroid dynamics, were successfully performed. The handheld microscope's compactness, ease of use, and cost-effectiveness render it a compelling alternative to high-grade incubator microscopes for routine, non-fluorescence cell culture studies, offering a paradigm shift towards pixel-optimized imaging throughput.

Keywords: live cell imaging, quantitative cell biology, high throughput imaging, low cost microscopy

Key points:

- Image through handheld microscope is four-fold higher than scientific camera (objective lenses)
- Handheld microscope can conduct single cell imaging in a cell incubator. Routinely imaging 2-3 thousand cells in a single field of view

1. Introduction

The use of cell culture incubators and optical microscopes are two of the most common scientific instruments in cell and tissue biology because they support a wealth of biophysical and biochemical experiments ranging from across cell cycle, tissue engineering, drug discovery and, immune activation. There are different ways to amalgamate these two technologies; they either involves fitting an incubator over an existing microscope or fitting a microscope into an existing incubator [1-5]. Here, we term these types of microscope as *incuscope*, an abbreviation of for **incu**bator-compatible micro**scope** technologies. All incuscopes are meant to continuously monitored the large population of cells undergoing proliferating and, dividing, death under strict environmental conditions (humidity, CO_2, temperature, cell culture media). A common feature of all incuscopes is the physical packaging of the microscope imaging system so that they are amenable to strict incubator environmental conditions (relative humidity-100%, CO_2-5%, temperature-37^oC). As a result, incuscopes often use consumer grade miniature optics (numerical aperture, ~0.01 to 0.2), illumination sources (i.e. light emitting diode) and miniature, high-definition CMOS imaging sensors (e.g. 3-5 megapixels).

The emergence of 3D tissue models (*i.e.* spheroid, tissue on chip and organoid) further amplify the need for incuscopes [1-4]. Recently, controlled three-dimensional (3D) tissue constructs, such as spheroids and organoids, have become essential for studying tissue development and multicellularity. These tissue constructs have significant implications for regenerative medicine, cancer metastasis, and tissue engineering [6-8]. Modelling cancer metastasis using spheroids with varying extracellular fluid and matrix can more accurately replicate the processes within the tumor microenvironment. It is necessary to therefore screen the integrity of spheroid rapidly[9]. Temporal imaging data helps to identify and quantify novel biological adaptation mechanisms over different growth phases, hence, the need to record spheroid volume growth kinetics over extended time period [10]. Extracellular environment play a major role in determining the types of 3D spheroids. Methyl-cellulose (MC) is a versatile material used in 3D spheroid growth because of low cytotoxicity, excellent biocompatibility, biodegradability, cell viability whilst do not trigger activation of cell adhesion molecule. In its gel phase, MC functions as an inert thickening agent, facilitating both the use of non-flat surfaces and soft biomaterials, to guide the production of homogenous spheroids [11]. On the other hand, in liquid phase, MC are reported to promote the migration of cancer [12]. The final results is to use handheld microscope to investigate the influence of MC on spheroid formation in the absence of a physical or soft materials. To do that, the handheld microscope would be

required to carry out continuous imaging of cells over several days. However, the factors determining imaging throughput in incuscopes are often overly focused on optical lens performance, rather than actual throughput.

This paper demonstrates that imaging throughput is not solely dependent on optical resolution or field of view (spatial bandwidth product). Instead, an *incuscope*'s performance should be evaluated by its ability to quantify distinguishable cells or spheroids within the available pixels, specifically the minimum number of pixels needed to capture a single cell. Here, we aim to evaluate the application of a consumer grade handheld microscope as an *incuscope*, with focus on imaging throughput. Here the throughput is defined by number of cells counted. The paper is divided into two main sections: one comparing the imaging performance, and the other focusing on its application to single cell tracking and spheroid biology. The imaging section compares throughput (pixel resolution and field of view) between a generic handheld microscope (Digitech, 5MP USB Digital Microscope), scientific grade microscope objective lens (Nikon) and digital camera (8 MP smartphone camera). The second part of the results focuses on the evaluation of handheld microscopes placed in an incubator without motorized stage for quantitative tracking and measurement of single cell movements [13-16] and spheroid formation and dissociation [17]. We investigate whether handheld microscopes offer adequate imaging resolution across their field of view to capture spheroid formation and cell invasion assays [18, 19] prior to the use of advanced 3D imaging-based pre-screening tools

2. Results

Incuscopes with a lower spatial bandwidth product can achieve higher imaging throughput that are optimal for live cell imaging applications.

SBP is the field of view (FOV) in mm^2 divided by the optical resolution (μm^2) that is directly affected by the choice of tube and relay lenses as well as any form of geometrical aberrations [20]. Recent advancements in microscopy imaging have mainly concentrated on enhancing resolution to increase the spatial product bandwidth (SBP). In live cell imaging, throughput is determined by the total number of cells that are resolved in a single frame under controlled conditions (humidity, temperature, CO2) rather than SBP. We argue that a high SBP does not directly correspond to the increased imaging throughput due to the constrained pixel density of the camera. The reason being that an efficient single cell imaging system should allocate the minimum number of pixels necessary to represent a single cell (ideally 4 $pixels^2$) rather than using a higher number of pixels for this purpose. A 4x objective lens will typically

provide a SBP of 2.7x 10^6 based on a single resolvable spot of 3.36 µm and a field of view of 5.5 mm . Given that many suspended and adherent mammalian cells typically range in diameter from 8 to 50 µm [21-23] the resolvable spot size of 3.36 µm significantly oversamples the dimension of a single cell.

Here we experimentally prove this by using calibrated resolution target and live cell samples [21-23]. We first proceed to quantify the difference in SBP [24, 25] and imaging throughput between a 4x objective lens (Olympus PLN) through a 10x magnification (eye piece) onto a 8 megapixel smartphone camera and a handheld microscope (Digitech 5MP USB Digital Microscope**,** JayCar Pty Ltd). Figure 1a) shows each imaging conducted with a USAF 1951 card, fixed pollen grain and live adherent cells in a thick culture flask. Figure 1a) [26]. Figure 1a) i) shows the imaging resolution measures at 3.91 µm with a field of view of 5.17 mm with a 4x objective lens (full field of view not shown). With this imaging resolution, we can clearly resolve a single pollen grain and single adherent cells. We then carried out the same test using the handheld microscope under both transmission (Figure 1a) ii)) and reflectance mode (Figure 1a) iii)). From our measurements, the transmitted imaging images from handheld microscope was able to cover a total field of view of 7.619 mm with resolvable features of 8.77 µm, approximately NA of 0.033 as shown in Figure. 1a) ii). This was sufficient to resolve single pollen grain, but was unable to resolve single cells due to light attenuation through the thick cell culture flask. On the other hand, for this specific handheld microscope model from Digitech, under reflectance mode the field of view was reduced to 5.750 mm whilst maintaining a lateral resolution of 8.77 µm, shown in Figure. 1a) iii). The handheld microscope is still capable of resolving single pollen grain and clearly resolving single adherent cells. Under reflectance imaging, there is minimal attenuation of light and therefore a low power LED was sufficient to image adherent cells clearly. As expected, the SBP of transmission brightfield microscope is 3 folds higher than handheld microscope in Figure. 1 b) i). A higher SBP typically demands lenses with finer spatial resolution, resulting in a smaller field of view and reduced imaging throughput. Instead, a low magnification system covers a large field of view which increases imaging throughput. The primary measure for imaging throughput is the minimum number of pixels required to distinguish an individual cell rather than the highest imaging resolution. For a given pixel area (256000 $pixel^2$), and to identify a single adherent fibroblast cell covering a physical area of 400 μm^2, a low magnification handheld microscope utilises only 64 $pixel^2$ (8 x 8) which is 6 folds less pixels than the 400 $pixel^2$ used in a transmission brightfield microscope. Figure 1 b) ii) and iii) shows that for the same pixel area, the throughput of a handheld microscope is already 4-fold higher than the microscope objective

(4x) used in transmission brightfield microscope. Figure 1b(ii)(top) displays the number of adherent cells captured within a 25,600 pixel² area using both a 4x microscope and a handheld microscope. Figure 1b(ii)(bottom) presents a cross-sectional intensity plots the reflectance imaging contrast of handheld microscope (signal to noise ratio- SNR ~1.4) against the transmitted imaging contrast of 4x objective lenses (SNR ~0.4). The reflectance image intensity of the handheld microscope is inverted for comparison. Because of the small form factor, the handheld microscope can easily fill into a compact incubator of only 30 litres. In comparison, the microscope using 4x objective requires an incubator of a size of 188 litres to fit, as shown in Fig. 1c) i) because of addition of condenser and tube lens. Because a 4x objective lens has a narrower field of view, a sample stage is needed to move the sample and capture the entire field of view. Conversely, a handheld microscope captures a larger field of view without the need to move the sample. Figure 1 shows that the inbuilt LED in the handheld microscope provide sufficient illumination when compared to a transmission brightfield microscope system to generate matching signal to noise ratio (between 1 ~ 2.5). A handheld microscope can quantify cell-sized particles, cover a larger area in one snapshot and can be used as a regular *incuscope*. To test the reliability, we proceed to carry out a ~ 12 months study where we continuously used the handheld microscope to perform the function of an *incuscope*.

By housing the handheld microscope in a compact cell culture incubator, shown in Figure. 1 c) ii)), we carried out a series of live cell imaging tasks. Since our study focuses the immediate application in cell biology, we did not address optical factors that influence imaging throughput, such as intermediate magnification lenses and the pixel size of the camera sensor. These aspects are covered by other mobile microscopy technologies. The handheld microscope are widely used to investigate cell migration [27], spheroid formation [28] and toxicity [29].

Can a handheld microscope reliably count cells in tissue culture flasks?

Tissue culture flasks are commonly used to grow different cell lines across various passages. Polymer walls of tissue culture flask typically measure several millimeters thick and is generally suited low magnification *incuscopes* which operates at a longer working distance. A performance criterion for *incuscopes* is their capability to monitor individual cells over several hours to days [4, 30-33] to quantitate cell number and morphology for each passage number. In this section, we use the handheld microscope image and count cell cultures in tissue culture flasks (T25, T75 Nunclon Delta flasks) over 16 hours period. Figure 2 shows images of murine cell lines grown in T75 flasks cultures using handheld microscope installed in the smaller incubator (Fig1 b i). Figure. 2 are images of murine cell lines- Figure 2 a) b) c) i) fibroblast (L-cell-L929, Passage 25), Figure 2 c) ii) ii) cancer cancer associated fibroblast (CAF) cells (Passage 30) and

Figure 2 c) iii) Pancreatic Ductal Adenocarcinoma (PDA) cells of the KPC mouse model, Passage 30, all cultured in T75 flask. Figure. 2a) i) show the full imaging field of view of the handheld microscope with 80% confluence. Four individual fields of view (1 to 4) were chosen using ImageJ (ROI manager) and are marked with red and blue circles. Each field of view (FOV) covers approximately 4 mm^2. Using ImageJ[34], a macro script was written to count cells. The macro encompasses three image processes, as shown in blue rectangular box: inversion of the look-up table (LUT), followed by edge detection, and finally, identification of the maximum intensities to determine the number of cells within each field of view [35]. Fig. 2 a) ii) Display cell counting using four FOVs: raw images (top row), maxima intensity images (bottom row), with counts of 774, 698, 903, and 892 cells. The total number of cell counts over the four selected field of views giving a cell density of 204 cells/mm^2. A manual check identified an error rate of about 5-8%. A video summary of the macro output is illustrated in *Supplementary Video 1*. The reported error in cell counting is less than 5%, which is consistent with other manual and automated cell counting methods [35]. *Supplementary Video 2* shows approximately 6000 cells imaged on regular cultures T25 flask monitored over 16 hours at 30 second intervals. The aggregated cell count is shown in Figure 1 b) which indicate a growth rate of 1.5 times per day. There were notable noise fluctuations, which can be attributed to changes in illumination intensity. For instance, around the 7.5-hour mark, these variations were likely caused by minor condensation on the LED surface. Longitudinal tracks of cell motility (L929) were conducted on sequence of images from handheld microscope as shown ain Fig. 2 c) using a general cell tracking software known as Trackmate [36] after image segmentation were conducted. Figure. 2 c) ii) and iii) showed two other cell types CAFs and PDA cells imaged at 70 and 20% confluence, video recordings are included in *supplementary Video 3.* Insets ii) and iii) of Figure 2 c) clearly show individual cell bodies.

Can low imaging resolution handheld microscopes identify cell division events?

We subsequently inquire whether a handheld microscope possesses adequate imaging resolution to quantify single-cell activities, such as migratory distance and direction, as well as to identify mitosis events [37]. Quantitative differences in various adherent cell types movement and division yield functional information about their physical behaviour on different microenvironment. Figure 3 a) i) and ii) shows representative images L929 cells (fibroblast) is seeded into a T25 flask for a period of 16 hours, under a handheld microscope and quantitative phase microscopy using a 20x objective lens [38]. Quantitative phase microscopy provides excellent imaging quality and high-resolution motility tracks (minimum tracking distance ~3

µm), but only 20 cells were tracked over 225 µm. The handheld microscope detects over 30 times more cells, n = 603 within ~1 mm, as shown in *Supplementary Video 3*. The maximum distance of migration for both images are around 170 µm in lateral distance. The handheld microscope demonstrated a higher cell count and produced a homogenous distribution of migration distances compared to a smaller field of view. It is noteworthy that the handheld microscope excelled in quantifying single-cell motility in cultures with lower confluence (< 40%). At lower confluency, we examined cell movement to identify cells undergoing different stages of mitosis. During mitosis, cells assume distinct morphology – cell rounding [39] that is observed under quantitative phase microscope [40, 41] as shown Fig. 3b) i). While under the handheld microscope, the rounding is not as clearly visible, but the subsequent cell splitting/division events can be easily tracked as shown in *Supplementary Video 5*. A video recording of from metaphase to telophase and cytokinesis [42] can be seen in the video. [43]. Our preliminary results (not shown) indicate the handheld microscope can measure aggregated cell growth to predict growth and is unable to identify all the cell division which is tied to imaging resolution (detecting cell rounding), After analysing image sequences over several passage number of the L929 cell type, the amount of multiplication rate is approximately 1.5-2 times per day that is comparable with other brightfield/phase contrast automated cell counting tools.

Can *handheld microscope* measure and compare 3D spheroid formation and dissociation rates?

A 3D culture protocol was developed based on the experimental observation that L929 cells express cell adhesion molecules (cadherin) when cultured in Dulbecco's Modified Eagle Medium (DMEM) without fetal bovine serum (FBS) - Supplementary Figure A1. The 3D model is used to investigate the role of MC in spheroid formation and dissociation. Specifically, we used L929 cells- a known cell line with low endogenous cell adhesion molecules. Our initial observation in fixed samples indicated that different MC solutions appear to modulate L929 spheroids packing density as shown in Supplementary Figure A2. The handheld microscope aim to reveal whether concentration of MC influences rate of spheroid formation and dissociation. Figure. 4a) shows the sequence of cell preparation. Cells were initially harvested from standard culture media (DMEM with 5% FBS) once they reached full confluence. They were then subjected to trypsinization, centrifugation, and washing before being re-seeded into viscosity DMEM (v_DMEM) without FBS. Two vDMEM solutions were made using MC concentrations of 1%, 2% respectively (Supplementary Protocol). After extended imaging and spheroid formation, the vDMEM culture is centrifuged and washed to remove vDMEM. The

culture is then resuspended in regular culture medium (DMEM + 10% FBS) for long-term monitoring of spheroid dissociation. Figure. 4 b) i) shows images taken from handheld microscope at Step 4 under different vDMEM solutions. The initial number of seeded cells is approximately 781,250 cells for a T25 flask. Figure 4b) i) also shows L929 cell readily organise into spheroids from 24 to 41 hours (1.7 days). Initial surface area measurements of the total number of cells show that cells from vDMEM-0, 1%, and 2% all aggregate into distinct spheroids within the first 24 hours. Figure 4b) ii) shows that cells in resuspended spheroids with DMEM+FBS began to spread and occupy space in the culture flask. Figure 4 c shows the surface area measurement in a single plot where the cell-cell aggregation occurs in the first 20 hours without FBS in all three different vDMEM solutions, whilst within the first 2 hours of being resuspended in DMEM+ FBS, the spheroid begun to dissociate rapidly. The dissociation rate indicates the difference of spheroid behaviour cultured in the different vDMEM solutions. We observed that with 0 to 1% vDMEM, the disassociation was similar, but at 2% we observed the total area reach a plateau. We therefore next determined the local cellular and spheroid morphological changes during the different phase of cell aggregation and dissociation. A handheld microscope do not support fluorescence signals, it is therefore necessary work out how images are further quantified to measure spheroid dynamics to determine the local cellular and spheroid morphological changes during the different phase of cell aggregation and dissociation. Figure 5 a) i) shows snapshot of cell and spheroid segmentation from threshold images captured by the handheld microscope, along with image analysis to measure cellular dynamics for individual spheroids at 0 and 40 hr period. For a selected imaging field of view, the segmentation process is used to measure spheroid area and circularity over 41 hours with different vDMEM solutions. Figure 5a) ii) and iii) show the time series plot of spheroid area and circularity, both increasing over time when cultured in the three vDMEM solutions (supplementary figure.A3) . The aggregated areas and circularities of the spheroids in the final 40 hours are presented in a bar graph. Although spheroid sizes vary greatly by area shown in Figure 5a) iv), their circularities are similar (0.7-1.0) as shown in Figure 5a) v). Further analysis of time lapse imaging, shown in Fig. 5b) i) and ii) indicates that each of the spheroid can independently migrate and the average migration speed of around 12 μm/hr. The migration of stromal spheroids might be associated with an increase in cadherin expressions [44].

Although the quantification of spheroid formation is straightforward, the same quantification step cannot be easily transfer to spheroid dissociation using the handheld microscope. This is because spheroid that are resuspended into DMEM+FBS solutions present more optical

challenges particularly optical turbidity i.e. uneven sample reflectivity. We resolved the issue by measuring the reflected light across specific spheroids, as shown in Figure 5c i) and ii). Figure 5c) i) shows the yellow line plot of a chosen spheroid versus the background. The linear intensity attenuation coefficient from this plot indicates the dissociation rate of the spheroid—smaller coefficients show complete cell dissociation, as illustrated in Figure 5c) ii). Figure 5 d) summaries the spheroids that grown under different vDMEM cultures after they have been resuspended in DMEM+FBS solution. Over the course of 40 hours, we observed the average dissociation rate of the 1% and 2% vDMEM is much slower than the 0% vDMEM, which can indicate an increase in cell-cell adhesion at the core of the spheroids. The initial results suggest that vDMEM of higher viscosity may yield tightly packed spheroids that persist and migrate. This may open up a new way to study the process of collective cell migration (tissue wetting-dewetting) and how viscosity drives the spontaneous migration of cell aggregates en masse. [45, 46]

3. Conclusion

In summary, we investigated the scientific integration of a commercially available handheld microscope within a compact commercial-grade cell incubator, effectively transforming it into a scientific incuscope. Our findings indicate that imaging throughput is not solely determined by imaging resolution and SBP. Instead, an incuscope's performance should be assessed based on its capacity to quantify distinguishable cells or spheroids within the available imaging pixels, specifically the minimum number of pixels required to capture a single cell. For instance, an incuscope equipped with a 5-megapixel camera should possess optical design to ensure that a grid of 9 by 9 pixels is utilized to image a single cell, which translates to approximately 280,000 cells being imaged within a single field of view. Essentially, the Nyquist sampling limits of an incuscope is measured by the smallest array of pixel used to image an individual cell. Whilst computational imaging technologies such as lensless microscopy [47] and Fourier Ptychography [48] directly map cells to pixels without relying on resolution/magnification of conventional optical lenses, these computational approaches often require minimal working distance or special illumination patterns that are often incompatible with thick imaging polymer walls of standard cell culturing flasks. Importantly, handheld microscope are packaged into a single imaging unit equipped with all the necessary illumination and imaging sensors along with software drivers (OpenCV) that can directly integrated with open-source micromanager program for single cell imaging. Our results further suggest that the reflectivity of cells and spheroids captured by a handheld microscope can be

digitally processed to investigate single-cell and spheroid dynamics, from cell migration and division to spheroid formation and dissociation. In addition, we anticipate that the handheld microscope can be used to also measure migration rate of cells from tumour spheroids invading into surrounding microenvironment. Next, we aim to expand the use of multiple handheld microscopes for capturing multi-well tissue culture plates, this will permit parallel imaging simultaneously. Commercial or open-source *incuscope* system [1] could leverage the importance of imaging throughput using lower numerical aperture optics and oblique-style reflectance imaging, to expand their applications into spheroid imaging. Through these quantitative cell biology experiments, an off-the-shelf handheld microscope is a highly attractive incuscope alternative that can readily serve the cell biology community.

Acknowledgement

Thank Melanie White from University of Queensland for the critical comments on the manuscript.

Figure. 1 –Imaging Throughput and Footprint

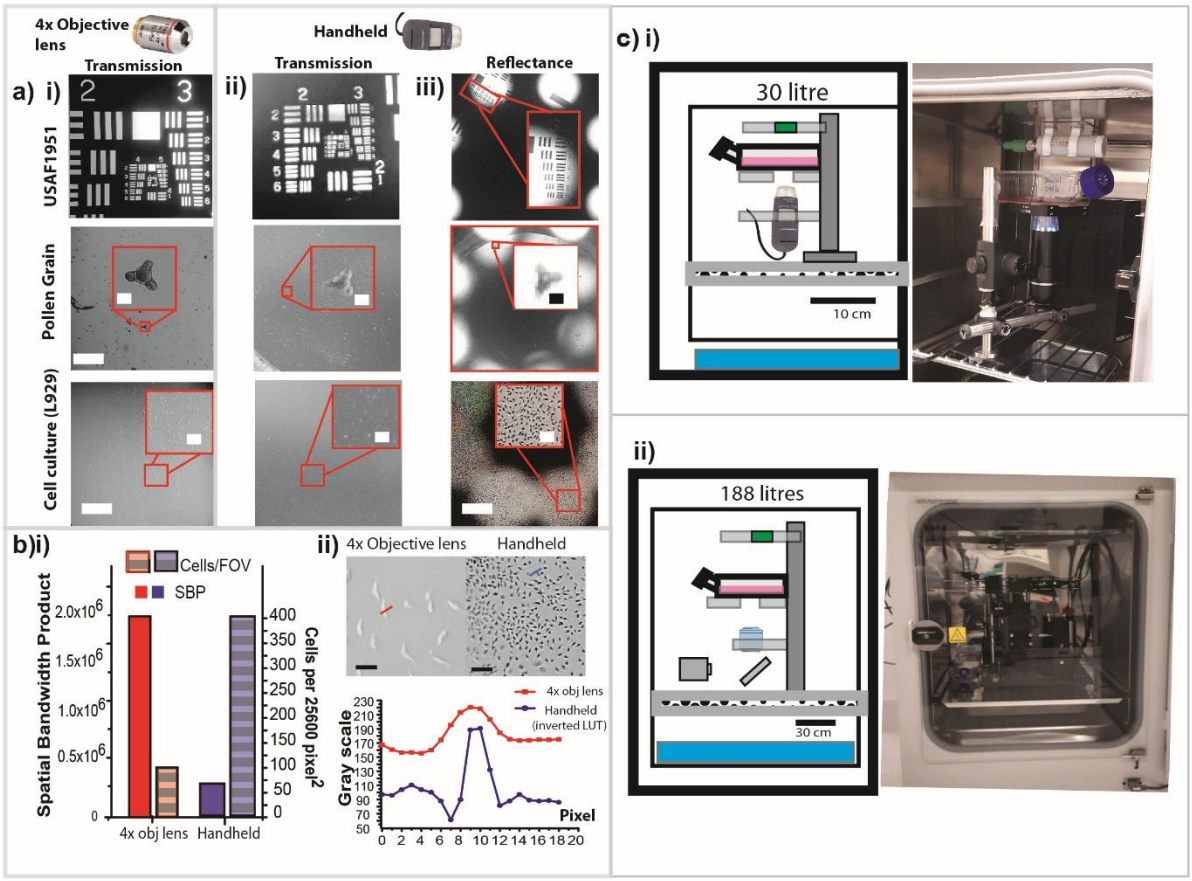

Figure 1 – Comparison of images quality, spatial bandwidth product and throughput of commercial microscope objective lens (Nikon TE2000, 4x objective lens and 10x eye piece magnification, 8 megapixels-OV08B) and handheld microscope (Digitech, 5MP USB Digital Microscope) with fixed and live samples- USAF1951, fixed pollen grain and live stromal cells (L929) cultured in T75 cell culture flask. a) i) transmittance images with objective lens, 4x, ii) transmittance images with a transilluminating LED through imaging sensor of the handheld microscope, iii) reflectance images acquired with in-built ring LED illuminator. b) i) bar plot that compares that for the same 25600 pixel^2 area – the spatial bandwidth product (SBP) and number of cells counted. ii) Images of L929 cell in T75 flask in the same 25600 pixel^2 area and comparing image intensities from an inverted microscope (red line) and the handheld microscope (blue line). c) i) Schematic of the cross section between a hand held microscope housed in cell incubator of 30 litre capacity and ii) an inverted microscope with 4x objective lenses housed in a cell culture incubator of 188 litre capacity. Scale bar a) i), ii), iii) _1000 µm, inset 50 µm. b) ii) 50 µm.

Figure 2 – Cell counting and Single cell Tracking

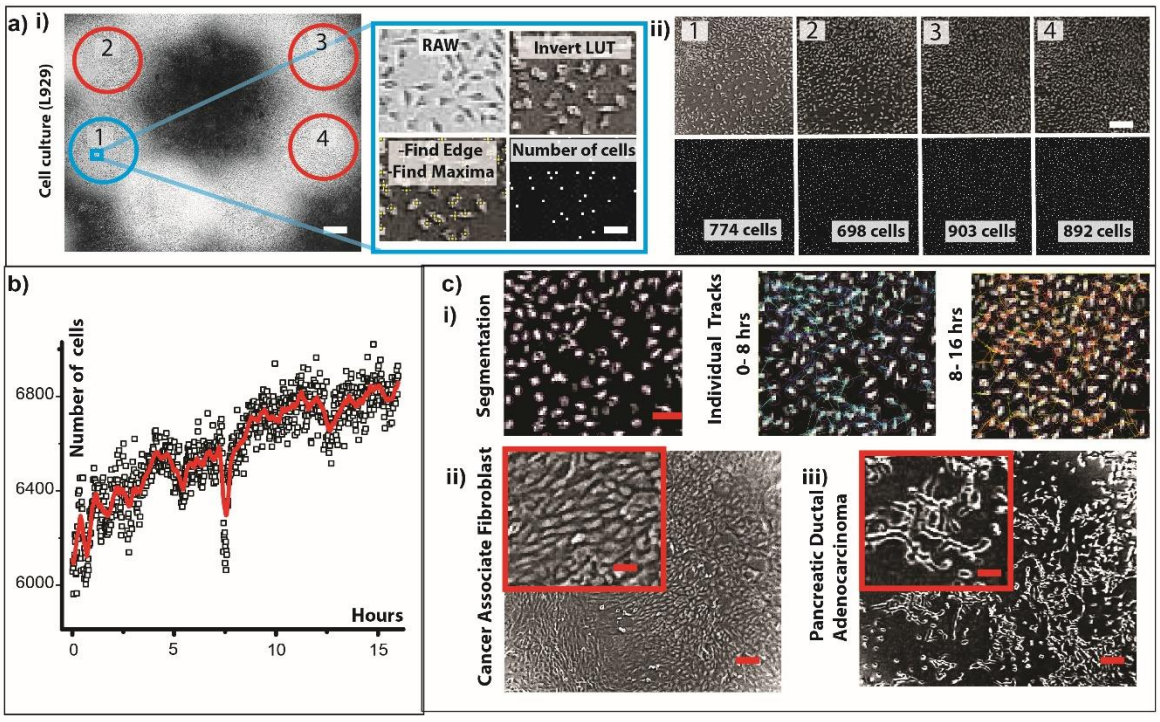

Figure 2 – a) i) shows the complete imaging field of view captured by the handheld microscope. Four individual fields of view, circled in red and blue and labeled 1, 2, 3, and 4, were selected for analysis. For cell counting, three post-processing steps were applied: invert LUT, find edge, and find maxima. First, the grayscale map of the raw reflectance image of the cells was inverted. Then, the find edge and find maxima steps were sequentially applied to count the number of cells within each field of view. ii) show the number of cells counted from four region of interest individually at the end of the first 16 hours of culturing. b) shows total number of cells from 1,2,3,4 field of views and the cumulative changes in cell numbers over the same 16 hourr time period. c) show an isolated field of view labelled 1 where images are first segmented, threshold and tracked using Trackmate in ImageJ to determine the individual migration paths of each cell over two 8 hours time interval (0 to 8 hrs and 8 to 16 hrs), c) ii) and iii) shows imaging of highly confluence (70%) cancer associated fibroblast line and pancreatic ductal adenocarcinoma cells cells from KPC model respectively. Scale bar a) i), ii)) 1000 µm, c) i), ii) ii) 200 µm. Inset 50 µm

Figure 3 – Migration and division

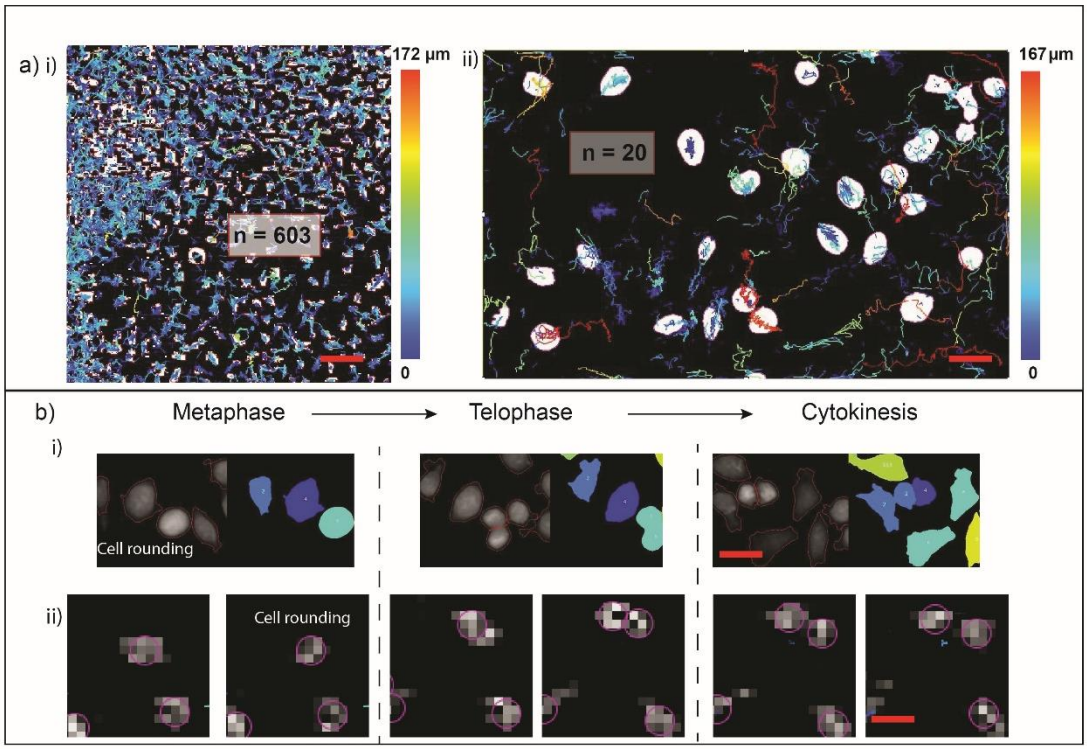

Figure. 3. a) Representative images of tracks of individual L929 cell are cultured on T25 Flask and glass bottom dishes i) handheld microscope - number of cells tracked (n)=603, and 4x objective lens - number of cells tracked (n) =20. Colored tracks indicate displacements. b) i) showing mitosis of cell from a quantitative phase microscope with a 10x objective lens and ii) handheld microscopy. Scale bar a) i) 100 µm ii)) 50 µm, b) i), ii) 20 µm.

Figure 4 – Imaging spheroid formation and dissociation

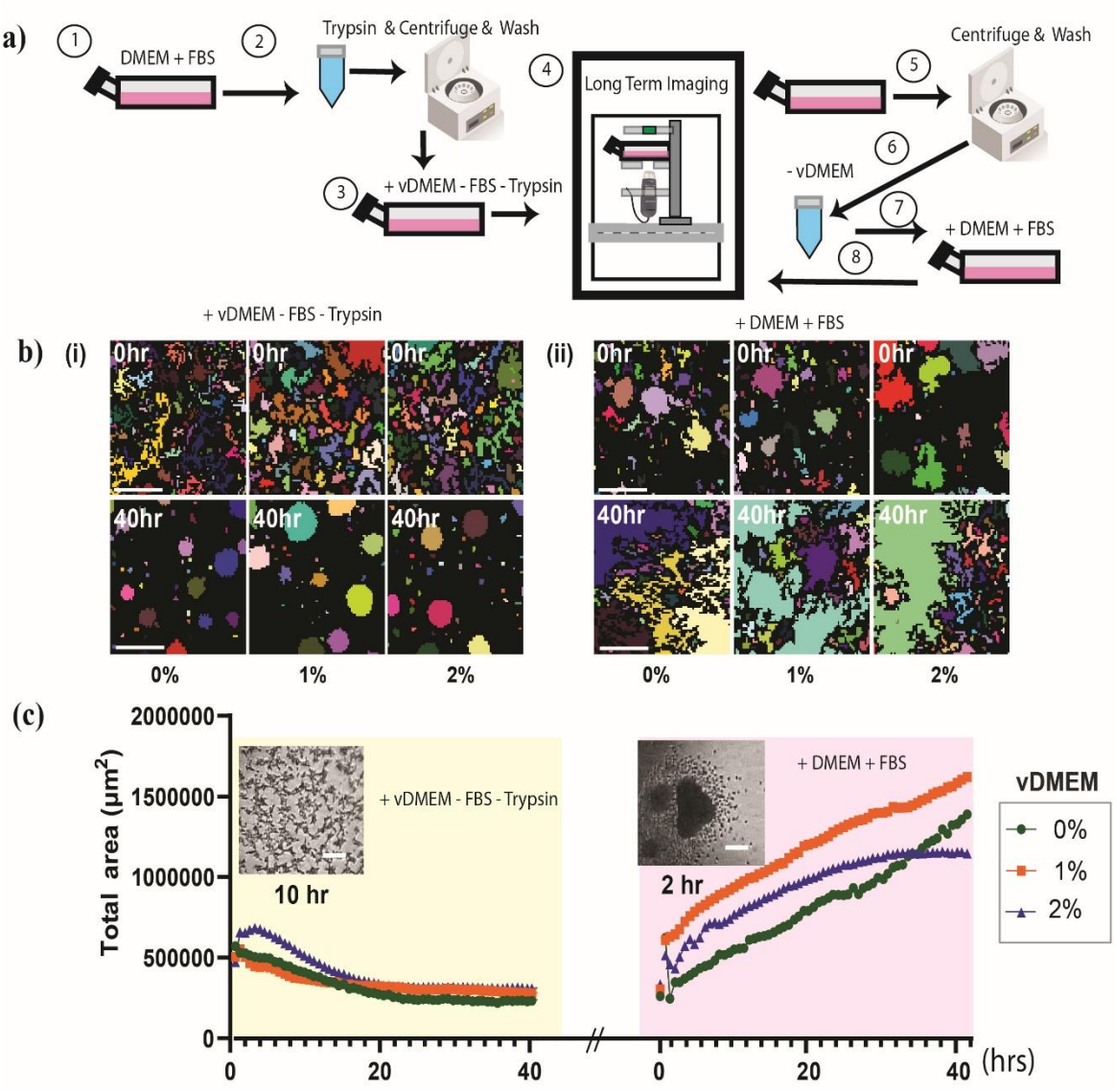

Figure. 4 a) spheroid formation: steps 1 to 4 that includes harvest and resuspend L929- adipose fibroblasts into viscous mixture of DMEM (vDMEM) for T25 Flask without FBS. Spheroid dissociation: Steps 5-8 to harvest and resuspend the spheroid into DMEM + FBS solution. Each imaging session in the incubator is 41 hours. b) representative image of the initial (0 hrs) and final conditions (40 hrs). Color indicate segmentation. c) time series plot of the total area quantified over 41 hours. Scale bar b) i), ii)) 100 µm, c) inset 100 µm.

Figure 5 –Quantification of spheroid dynamics using handheld microscope

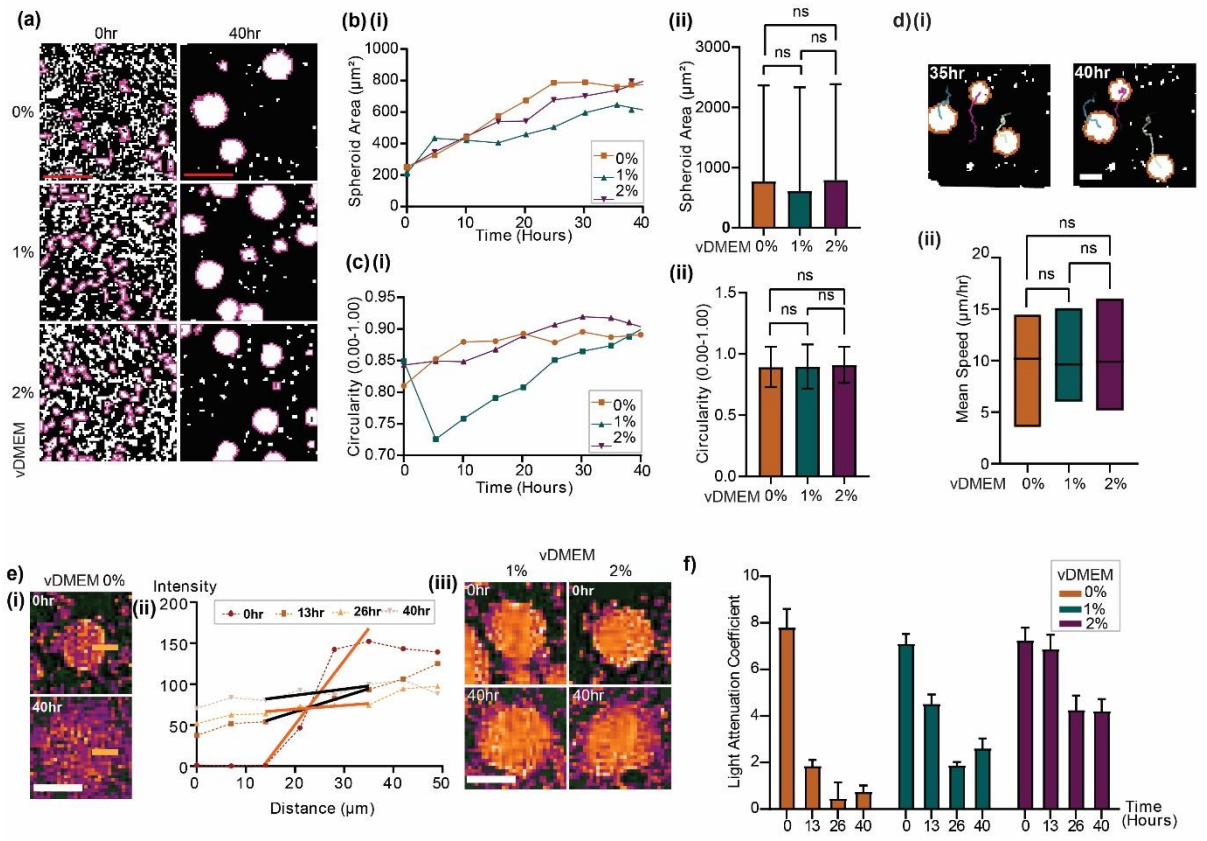

Figure. 5 –(a) i) Representative images of the use of circularity filter from TrackMate Filter (Circularity ≥0.23- criterion) used to extract spheroids from cell cultured in all vDMEM conditions at 0hr and 40hr. Each purple outline identifies cell aggregates which met the criteria**. (b)(i) and (ii)** Longitudinal changes to the size of aggregate (µm^2) and circularity across the 40-hour culture for vDMEM conditions (N spheroids=12). Each data point are calculated mean values from 12 spheroids**. b)ii)** Final size of aggregate (µm^2) after 40-hours for 0% (n=431), 1% (n=575) and 2% (n=569) vDMEM. Unpaired T-tests indicated no significant difference in final aggregate size between vDMEM conditions. Data represented as mean±s.d. **(c)(i)** Circularity (0.00-1.00) of individual spheroids across 40-hour culture for all vDMEM conditions (N spheroids=12). Data represented as mean values of 12 spheroids. **c) (ii)** plots the final circularity (0.00-1.00) of aggregates after 40-hour culture for 0% (n=656), 1% (n=714) and 2% (n=696) vDMEM. Unpaired T tests indicated no significant difference in final aggregate circularity between vDMEM conditions. Data represented as mean values±s.d. **d)i)** Representative images of spheroid migration over ≥10 hours for 0% DMEM at 35hr and 40hr. Orange outline identifies spheroids and corresponding migration paths (purple, green lines). **d) ii)** Average speed of spheroids (µm/hr) between 30 - 40hrs for vDMEM conditions 0% (n=42), 1% (n=29), and 2% (n=35). Unpaired T- tests revealed no significant difference in mean speed of spheroids travelling under all the vDMEM conditions. **e) i**) Dissociation of stromal spheroids is marked by the intensity gradient (light attenuation coefficient) measured along the orange line (50µm in length). **e) ii)** Plot of raw intensity along with a linear regression (thick line – black and orange). Simple linear regression was used to fit intensity gradient (distance 14-35µm) (e.g. Slope = 7.178, R2 = 0.9745). **e) iii)** shows intensity of spheroids developed in all the vDMEM immediately (0hr) and 40-hours (40hr) after resuspension resuspended in DMEM+FBS. **f)** Light attenuation coefficient from linear regression resuspension for spheroids previous developed in vDMEM across 0hr, 13hr, 26hr and 40hrs. All profiles had R-squared value of ≥0.8, except from 0% at 26hr and 0% at 40hr. Two-tailed p-value of slopes indicated that difference of slopes within vDMEM conditions 0% ($p<0.0001$), 1% ($p<0.0001$) and 2% ($p=0.0007$) were statistically significant. Data represented are mean±s.d. a) Scale bars represent 200µm. d), e) 100µm.

Table 1 – Comparison of incubator microscope

Microscope	Cost	Integrated lighting	Industry package	microManager Compaitbiliy
DIGITECH (paper)	AUD$300	Yes	Yes	Yes
INCUYTE	AUD$25,000*	Yes	Yes	No
CM30	AUD$10,000*	Yes	Yes	No

*- estimates

Supplementary Files

A) Supplementary Figures
- Figure. A1 - Cadherin expressed in L929 spheroid after culturing in 0%, 1%, 2% vDMEM without fetal bovine serum
- Figure A2 - Representative images of spheroid formation with vDMEM 1%, 2%
- Figure A3 - Intensity gradient (light attenuation coefficient) measured for each vDMEM solution

B) Video 1 – Cell Counting
C) Video 2 – Imaging L929 cells over 16 hours at 60 second intervals
D) Video 3 – Single cell tracking L929 migration over 3hrs using trackmate
E) Video 4 – Seeding KPC cells on T75 flask
F) Video 5- Mitosis of L929 with quantitive microscopy and handheld microscope
G) Video 6 – Tracking of spheroid movement in 1% vDMEM
H) Protocol to prepare Methyl-Cellulose (MC)
I) Protocol for spheroid formation
J) Protocol for spheroid dissociation

References

1. J. Salido, G. Bueno, J. Ruiz-Santaquiteria and G. Cristobal, *Microscopy Research and Technique*, 2022, **85**, 3270-3283.
2. A. C. Zehrer, A. Martin-Villalba, B. Diederich and H. Ewers, *Journal*, 2023, DOI: 10.1101/2023.05.31.542706.
3. M. P. Walzik, V. Vollmar, T. Lachnit, H. Dietz, S. Haug, H. Bachmann, M. Fath, D. Aschenbrenner, S. Abolpour Mofrad, O. Friedrich and D. F. Gilbert, *Biosensors and Bioelectronics*, 2015, **64**, 639-649.
4. D. Jin, D. Wong, J. Li, Z. Luo, Y. Guo, B. Liu, Q. Wu, C.-M. Ho and P. Fei, *Scientific Reports*, 2015, **5**, 18483.
5. A. C. Zehrer, A. Martin-Villalba, B. Diederich and H. Ewers, *eLife*, 2024, **12**, RP89826.
6. C. M. Leung, P. de Haan, K. Ronaldson-Bouchard, G.-A. Kim, J. Ko, H. S. Rho, Z. Chen, P. Habibovic, N. L. Jeon, S. Takayama, M. L. Shuler, G. Vunjak-Novakovic, O. Frey, E. Verpoorte and Y.-C. Toh, *Nature Reviews Methods Primers*, 2022, **2**, 33.
7. E. Fennema, N. Rivron, J. Rouwkema, C. van Blitterswijk and J. de Boer, *Trends in Biotechnology*, 2013, **31**, 108-115.
8. K. Duval, H. Grover, L.-H. Han, Y. Mou, A. F. Pegoraro, J. Fredberg and Z. Chen, *Physiology*, 2017, **32**, 266-277.
9. J. Friedrich, C. Seidel, R. Ebner and L. A. Kunz-Schughart, *Nature Protocols*, 2009, **4**, 309-324.
10. R. J. Murphy, G. Gunasingh, N. K. Haass and M. J. Simpson, *PLOS Computational Biology*, 2023, **19**, e1010833.
11. S. M. Maritan, E. Y. Lian and L. M. Mulligan, *JoVE*, 2017, DOI: doi:10.3791/55544, e55544.
12. K. Bera, A. Kiepas, I. Godet, Y. Li, P. Mehta, B. Ifemembi, C. D. Paul, A. Sen, S. A. Serra, K. Stoletov, J. Tao, G. Shatkin, S. J. Lee, Y. Zhang, A. Boen, P. Mistriotis, D. M. Gilkes, J. D. Lewis, C.-M. Fan, A. P. Feinberg, M. A. Valverde, S. X. Sun and K. Konstantopoulos, *Nature*, 2022, **611**, 365-373.
13. V. Ulman, M. Maška, K. E. G. Magnusson, O. Ronneberger, C. Haubold, N. Harder, P. Matula, P. Matula, D. Svoboda, M. Radojevic, I. Smal, K. Rohr, J. Jaldén, H. M. Blau, O. Dzyubachyk, B. Lelieveldt, P. Xiao, Y. Li, S.-Y. Cho, A. C. Dufour, J.-C. Olivo-Marin, C. C. Reyes-Aldasoro, J. A. Solis-Lemus, R. Bensch, T. Brox, J. Stegmaier, R. Mikut, S. Wolf, F. A. Hamprecht, T. Esteves, P. Quelhas, Ö. Demirel, L. Malmström, F. Jug, P. Tomancak, E. Meijering, A. Muñoz-Barrutia, M. Kozubek and C. Ortiz-de-Solorzano, *Nature Methods*, 2017, **14**, 1141-1152.
14. E. M. B. Quinsgaard, M. S. Korsnes, R. Korsnes and S. A. Moestue, *Experimental Cell Research*, 2024, **437**, 113993.
15. F. Buggenthin, C. Marr, M. Schwarzfischer, P. S. Hoppe, O. Hilsenbeck, T. Schroeder and F. J. Theis, *BMC Bioinformatics*, 2013, **14**, 297.
16. I. Belyaev, J.-P. Praetorius, A. Medyukhina and M. T. Figge, *Cytometry Part A*, 2021, **99**, 1218-1229.
17. S.-E. Kim, S. Y. An, D.-H. Woo, J. Han, J. H. Kim, Y. J. Jang, J. S. Son, H. Yang, Y. P. Cheon and J.-H. Kim, *Stem Cells and Development*, 2013, **22**, 1818-1829.
18. M. Lemmens, B. Fischer, M. Zogg, L. Rodrigues, G. Kerr, A. del Rio-Espinola, F. Schaeffer, D. Maddalo, V. Dubost, A. Piaia, A. Mueller, U. Plappert-Helbig, U. Naumann, J. Haegele, A. Odermatt, H.-J. Martus and S. Libertini, *Molecular Therapy Methods & Clinical Development*, 2021, **23**, 241-253.
19. M. Vinci, C. Box and S. A. Eccles, *JoVE*, 2015, DOI: doi:10.3791/52686, e52686.
20. O. S. Cossairt, D. Miau and S. K. Nayar, *J. Opt. Soc. Am. A*, 2011, **28**, 2540-2553.
21. W. M. Lee, A. Upadhya, P. J. Reece and T. G. Phan, *Biomed. Opt. Express*, 2014, **5**, 1626-1635.
22. J. S. Cybulski, J. Clements and M. Prakash, *PLOS ONE*, 2014, **9**, e98781.
23. N. A. Switz, M. V. D'Ambrosio and D. A. Fletcher, *PLOS ONE*, 2014, **9**, e95330.

24. A. W. Lohmann, R. G. Dorsch, D. Mendlovic, Z. Zalevsky and C. Ferreira, *J. Opt. Soc. Am. A*, 1996, **13**, 470-473.
25. J. Park, D. Brady, G. Zheng, L. Tian and L. Gao, *Advanced Photonics*, 2021, **3**, 044001.
26. D. N. Breslauer, R. N. Maamari, N. A. Switz, W. A. Lam and D. A. Fletcher, *PLOS ONE*, 2009, **4**, e6320.
27. C. Fan, X. Shi, K. Zhao, L. Wang, K. Shi, Y.-J. Liu, H. Li, B. Ji and Y. Jiu, *Journal of Cell Biology*, 2022, **221**.
28. H. Baba, T. Fujita, K. Mizuno, M. Tambo and S. Toda, *ACS Synthetic Biology*, 2024, **13**, 1705-1715.
29. V. Cannella, R. Altomare, G. Chiaramonte, S. Di Bella, F. Mira, L. Russotto, P. Pisano and A. Guercio, *BioMed Research International*, 2019, **2019**, 3469525.
30. G. O. T. Merces, C. Kennedy, B. Lenoci, E. G. Reynaud, N. Burke and M. Pickering, *HardwareX*, 2021, **9**, e00189.
31. J. Kim, B. M. Henley, C. H. Kim, H. A. Lester and C. Yang, *Biomed. Opt. Express*, 2016, **7**, 3097-3110.
32. R. Sciorio, J. K. Thong and S. J. Pickering, *Journal of Assisted Reproduction and Genetics*, 2018, **35**, 515-522.
33. A. Zweifach, *Journal of Cell Biology*, 2024, **223**, e202401074.
34. A. Edelstein, N. Amodaj, K. Hoover, R. Vale and N. Stuurman, *Current Protocols in Molecular Biology*, 2010, **92**, 14.20.11-14.20.17.
35. I. V. Grishagin, *Analytical Biochemistry*, 2015, **473**, 63-65.
36. J.-Y. Tinevez, N. Perry, J. Schindelin, G. M. Hoopes, G. D. Reynolds, E. Laplantine, S. Y. Bednarek, S. L. Shorte and K. W. Eliceiri, *Methods*, 2017, **115**, 80-90.
37. D. Mohammed, G. Pardon, M. Versaevel, C. Bruyère, L. Alaimo, M. Luciano, E. Vercruysse, B. L. Pruitt and S. Gabriele, *Cellular and Molecular Bioengineering*, 2020, **13**, 87-98.
38. Z. Zhang, Y. Zheng, T. Xu, A. Upadhya, Y. J. Lim, A. Mathews, L. Xie and W. M. Lee, *Biomed. Opt. Express*, 2020, **11**, 5478-5487.
39. C. Cadart, E. Zlotek-Zlotkiewicz, M. Le Berre, M. Piel and Helen K. Matthews, *Developmental Cell*, 2014, **29**, 159-169.
40. X. He, C. V. Nguyen, M. Pratap, Y. Zheng, Y. Wang, D. R. Nisbet, R. J. Williams, M. Rug, A. G. Maier and W. M. Lee, *Biomed. Opt. Express*, 2016, **7**, 3111-3123.
41. X. Liu, S. Oh, L. Peshkin and M. W. Kirschner, *Proceedings of the National Academy of Sciences*, 2020, **117**, 27388-27399.
42. A. Bruce, *Molecular biology of the cell*, Second edition. New York : Garland Pub., [1989] ©1989, 1989.
43. S. Kamlund, D. Strand, B. Janicke, K. Alm and S. Oredsson, *Cell Cycle*, 2017, **16**, 2128-2138.
44. K. M. Mrozik, O. W. Blaschuk, C. M. Cheong, A. C. W. Zannettino and K. Vandyke, *BMC Cancer*, 2018, **18**, 939.
45. G. Beaune, C. Blanch-Mercader, S. Douezan, J. Dumond, D. Gonzalez-Rodriguez, D. Cuvelier, T. Ondarçuhu, P. Sens, S. Dufour, M. P. Murrell and F. Brochard-Wyart, *Proceedings of the National Academy of Sciences*, 2018, **115**, 12926-12931.
46. M. Mathieu, A. Isomursu and J. Ivaska, *Journal of Cell Science*, 2024, **137**.
47. G. Kuo, F. Linda Liu, I. Grossrubatscher, R. Ng and L. Waller, *Opt. Express*, 2020, **28**, 8384-8399.
48. G. Zheng, R. Horstmeyer and C. Yang, *Nature Photonics*, 2013, **7**, 739-745.